PCCP

ROYAL SOCIETY OF CHEMISTRY

PAPER

View Article Online
View Journal

Cite this: DOI: 10.1039/d6cp00960c

Solvent identity reshapes the conformational ensemble of a group-3 LEA model peptide

Itzel Pérez-Trejo and Laura Dominguez *

Group-3 late embryogenesis abundant (LEA) proteins are intrinsically disordered proteins (IDPs) that protect cellular components during desiccation. Their transition from disordered to ordered conformations is driven by reduced water availability. Here, we characterize and compare the conformational ensembles of the P1LEA-22 model peptide in TFE–water and glycerol–water mixtures that mimic distinct dehydration environments. Using Gaussian accelerated molecular dynamics (GaMD), we sampled the structural landscape of P1LEA-22 at 20%, 40%, 60%, and 80% cosolvent concentrations. The simulations provide an atomistic description of how solvent composition and water availability reshape peptide folding. We show that the conformational ensemble depends strongly on solvent identity and concentration. TFE acts as a helix-inducing cosolvent; at 80%, it stabilizes a compact helix–turn–helix motif through enhanced intrahelical electrostatic interactions, driven by hydrophobic shielding from TFE fluorine atoms. In contrast, glycerol promotes compaction through steric restriction and competitive solvation, leading to structurally heterogeneous ensembles that include β-sheet-like conformations and centrally localized helices. Although both solvents mimic dehydration, they modulate the peptide's energy landscape through distinct mechanisms: TFE couples hydrophobic association and electrostatic reinforcement to cooperative helix stabilization, whereas glycerol drives global compaction *via* excluded volume and hydrogen-bond redistribution. These findings provide molecular-level insight into how LEA proteins adapt structurally under water-deprived conditions.

Received 15th March 2026,
Accepted 11th June 2026

DOI: 10.1039/d6cp00960c

rsc.li/pccp

1 Introduction

In recent years, late embryogenesis abundant (LEA) proteins have attracted increasing attention due to their intrinsically disordered nature and their essential role in cellular tolerance to extreme dehydration. First identified in cotton seeds,[1] LEA proteins are highly expressed during late embryogenesis and in vegetative tissues under water stress conditions.[2–4] These proteins are typically highly hydrophilic, characterized by a high glycine content and a low abundance of hydrophobic residues,[5] features that are closely linked to their conformational plasticity and functional adaptability. In aqueous environments, LEA proteins generally remain structurally disordered. However, reduced water availability promotes the formation of ordered secondary-structure elements, highlighting their strong sensitivity to solvent conditions.[6]

LEA proteins are classified into seven groups based on sequence similarity and conserved motifs.[7] Among them, Group-3 LEA proteins are particularly notable for their ability to protect enzymes such as lactate dehydrogenase (LDH),[8] citrate synthase, and phosphofructokinase[9] under dehydration stress by preventing irreversible aggregation. A defining feature of Group-3 LEA proteins is the presence of conserved 11-residue repeat motifs, in which several positions are preferentially occupied by charged amino acids.[10] To isolate the functional role of these motifs, short model peptides derived from the 11-mer repeats have been synthesized and extensively characterized. These peptides reversibly adopt α-helical conformations under dehydrating conditions and return to disordered states upon rehydration, supporting the hypothesis that structural responsiveness is central to their protective function.[11] Moreover, physicochemical parameters such as peptide length, composition, concentration, and protonation state critically modulate their ability to suppress aggregation of proteins,[12] lipid assemblies,[13] and enzymes[14] during desiccation. In some cases, these model peptides protect protein function more effectively than classical protectants such as trehalose.[15]

Experimentally, dehydration is often mimicked using cosolvents that reduce water accessibility or activity and alter the dielectric properties of the solvent environment. Among these, 2,2,2-trifluoroethanol (TFE) is widely employed due to its strong propensity to stabilize α-helical structures by promoting intramolecular hydrogen bonds.[16] Beyond its helix-inducing effect, TFE has been shown to act as a nanocrowder, with local clustering influencing peptide conformational equilibria. Fourier-transform infrared spectroscopy studies have demonstrated that while certain intrinsically disordered peptides,

Departamento de Fisicoquímica, Facultad de Química UNAM, CDMX, Mexico.
E-mail: lauradd@unam.mx; Fax: +52 5556223773; Tel: +52 5556223773

such as phosphorylated kinase-inducible domain (pKID), exhibit great TFE-dependent conformational changes, LEA-derived peptides display a remarkable insensitivity to TFE concentration.[17] In contrast, glycerol serves as a more physiologically relevant mimic of intracellular crowding during dehydration, stabilizing α-helical conformations through excluded-volume effects and altered solvent viscosity rather than direct helix induction.[18,19]

From a computational perspective, capturing the full conformational landscape of disordered LEA model peptides in mixed solvent environments poses a significant challenge for conventional molecular dynamics (MD) simulations due to slow convergence and the presence of multiple shallow free-energy minima. Gaussian accelerated molecular dynamics (GaMD) offers an efficient, unconstrained enhanced-sampling approach that enables the recovery of the underlying free-energy landscape without predefined reaction coordinates. In previous work, we demonstrated that GaMD does not significantly perturb the physical properties of TFE–water mixtures, supporting its use for mixed-solvent simulations.[20] Here, we adapt this framework to peptide-containing TFE–water and glycerol–water systems to determine how solvent identity reshapes the conformational ensemble of a Group-3 LEA model peptide.

In this work, we employ GaMD simulations to characterize and compare the conformational ensembles of the P1LEA-22 model peptide in TFE–water and glycerol–water mixtures. By providing an atomistic description of how solvent composition and water availability reshape the peptide's structural landscape, we elucidate the distinct roles of helix induction, crowding, and solvation in modulating disorder-to-order transitions. This comparative analysis offers fundamental insight into the biophysical mechanisms that enable Group-3 LEA proteins to preserve macromolecular integrity under extreme dehydration conditions.

2 Materials and methods

To investigate how water availability affects the structure of the P1LEA-22 model peptide, the peptide was simulated in TFE–water and glycerol–water mixtures at four cosolvent concentrations: 20% v/v, 40% v/v, 60% v/v, and 80% v/v. Additionally, comprehensive step-by-step description of the operational parameters, optimization sequence, and specific role of each computational tool used in this workflow is provided in the SI as a methodological workflow summary.

2.1 Preparation and equilibration of cosolvent mixtures

Small solvent boxes containing water and the desired molar fraction of TFE or glycerol were first constructed. These systems are referred to here as unit boxes. Using Packmol,[21] the appropriate number of water and cosolvent molecules was placed inside a cubic simulation cell. Force-field parameters for TFE and glycerol were generated using the Antechamber module[22] and described with the general amber force field 2 (GAFF2).[23] Water molecules were modeled using the TIP4P-D four-point model.[24] Each unit box was minimized using 1 000 steps of steepest descent followed by conjugate gradient minimization. The systems were then heated from 0 K to 298 K and equilibrated for 10 ns. After equilibration, 50 ns production simulations were carried out at 298 K and 1 bar. While this setup follows the construction protocol described in our previous work,[20] all molecular dynamics simulations and resulting trajectories reported in this study were generated for this work.

All simulations were performed using the AMBER18 package.[25] A 2 fs time step was employed, and all bonds involving hydrogen atoms were constrained using the SHAKE algorithm.[26] Long-range electrostatic interactions were treated using the particle mesh Ewald (PME) method,[27] and an 8 Å cutoff was applied for nonbonded interactions. Temperature was controlled using Langevin dynamics[28] with a collision frequency of 2.0 ps^{-1}, and pressure was regulated using the Berendsen barostat.

2.2 Construction of peptide–solvent systems

After equilibration, twelve unit boxes were assembled in a 2 × 2 × 3 arrangement to construct the final solvent environment. The initial peptide structure was generated from its sequence (Fig. 1) using the I-TASSER server.[29] The peptide was inserted into the pre-equilibrated solvent matrix while maintaining a minimum distance of 6 Å between the peptide and the boundaries of the solvent box (Fig. 2). The complete systems were parameterized using Antechamber,[22] and the peptide was described with the Amber99SB*-ILDN force field.

2.3 Molecular dynamics simulations

The peptide–solvent systems were first equilibrated for 10 ns using Gaussian accelerated molecular dynamics (GaMD) at constant temperature. A short conventional molecular dynamics (cMD) simulation of 0.4 ns was subsequently performed at constant pressure and temperature to stabilize the system volume. Production simulations were then carried out using GaMD for 1 μs at 298 K and 1 bar, employing the same simulation parameters described for the unit boxes. GaMD simulations used a dual-boost potential in which acceleration potentials were applied to both the dihedral and total potential energy terms. The threshold energy was set to the lower bound for both boost potentials, and the GaMD parameters were updated every 0.4 ns to ensure accurate estimates of the potential statistics.

Free-energy profiles were obtained through energetic reweighting using the PyReweighting toolkit.[30] The reweighting procedure employed a Maclaurin series expansion up to the 10th order to account for the large energy fluctuations of the

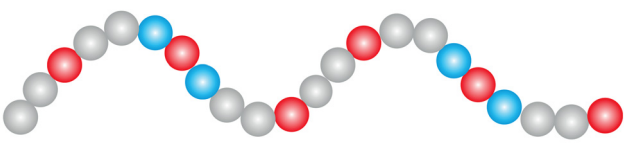

Fig. 1 Sequence of the P1LEA-22 model peptide.

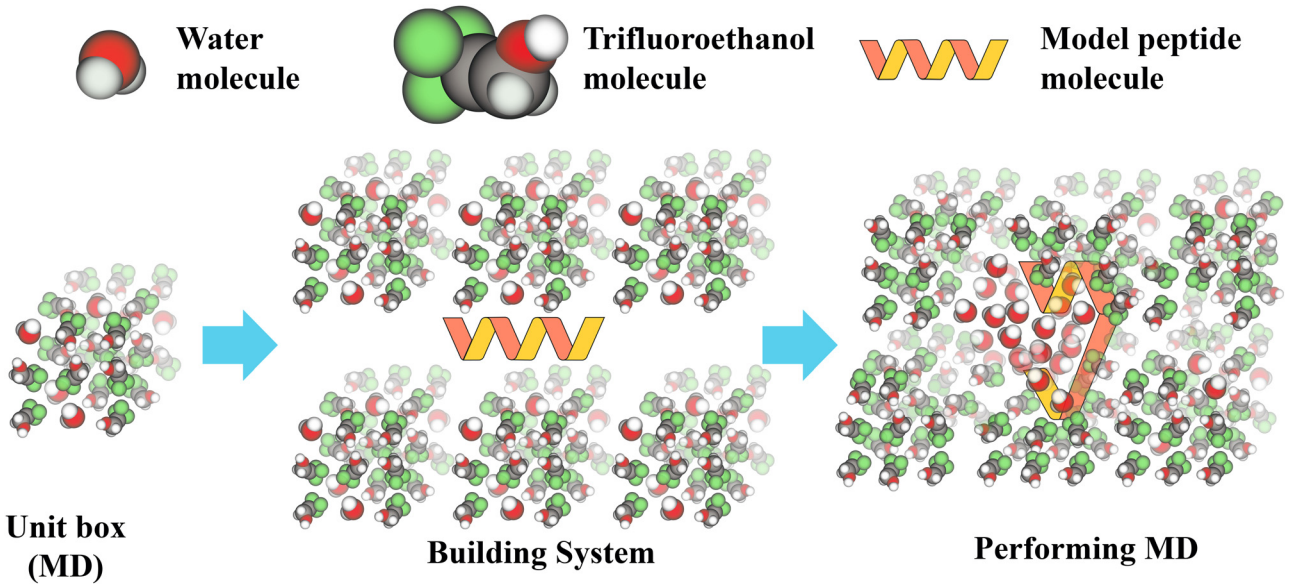

Fig. 2 System setup from the *unit box* to the full assembly and subsequent molecular dynamics simulations. Glycerol-based systems were constructed following the same workflow.

system. Structural stability and equilibration were evaluated by analyzing the time evolution of the radius of gyration (R_g) for all trajectories. Stabilization of R_g fluctuations and the absence of long-term drift indicate that the systems reached steady conformational regimes prior to analysis. Representative R_g time traces are provided in the SI (Fig. S1 and S2).

2.4 Molecular dynamics validation

To assess whether the structural trends observed in GaMD simulations arise from enhanced sampling rather than artifacts of the boost potential, additional conventional molecular dynamics (cMD) simulation were performed. One representative solvent condition (80% TFE) was simulated for 5 μs at 298 K and 1 bar using the same force-field parameters and simulation settings described above, but without applying the GaMD boost potential. To evaluate the robustness of our findings across all conditions, the remaining systems were validated using cMD trajectories of 2 μs (Fig. S4 in the SI).

The radius of gyration (R_g) and N–C terminal distance (d_{ee}) distributions obtained from the cMD trajectory were compared with those obtained from GaMD simulations. The agreement between the R_g and d_{ee} distributions indicates that the enhanced sampling protocol does not introduce artificial structural bias and accurately captures the underlying conformational landscape (Fig. S3 in the SI).

3 Results

3.1 Effect of the cosolvent in the free-energy surfaces

The free-energy surfaces, expressed as a function of the radius of gyration (R_g) and the N–C terminal distance, define the dominant low-energy conformational states of the peptide. As illustrated in Fig. 3, these surfaces evolve with increasing cosolvent concentration from left to right (20%, 40%, 60%, and 80%), where the top row represents TFE–water mixtures and the bottom row depicts glycerol–water.

3.1.1 TFE–water mixtures. *Concentration-dependent conformational evolution*. At 20% TFE–water (Fig. 3, top left), the free-energy surface shows minima at N–C terminal distances between 30 and 35 Å and radii of gyration between 11 and 13 Å. The global minimum corresponds to a largely disordered structure. At 40% TFE–water (top row, second column), the landscape shifts toward slightly more compact states, with minima characterized by N–C terminal distances of 20–35 Å and radii of gyration between 10 and 12 Å. Structured fragments begin to emerge at this concentration and predominantly adopt α-helical conformations. At 60% TFE–water (top row, third column), the surface displays multiple minima with terminal distances ranging from 15 Å to 30 Å. At 80% TFE–water (top row, far right), the landscape becomes dominated by compact conformations. A prominent minimum occurs at N–C distances below 10 Å and approximately 9 Å in R_g, corresponding to a stabilized type of helix–turn–helix structure. As TFE concentration increases, the ensemble progressively enriches in compact, α-helical states.

Fig. 3 shows a clear concentration-dependent shift in TFE–water mixtures from disordered and extended conformations toward compact states with stabilized α-helical architecture.

3.1.2 Glycerol–water mixtures. *Compaction and structural heterogeneity*. Fig. 3 reveals a distinct progression in glycerol–water mixtures. At 20% glycerol–water (bottom left), the low-energy conformations shift toward more compact states relative to 20% TFE–water, with radii of gyration between 8 and 11 Å and N–C terminal distances between 20 and 35 Å. Both extended and compact conformations coexist within the energetically favorable ensemble. At 40% glycerol–water (bottom row, second column), the landscape shows minima similar in overall dimensions to those in TFE; however, an additional compact minimum appears with an N–C terminal distance

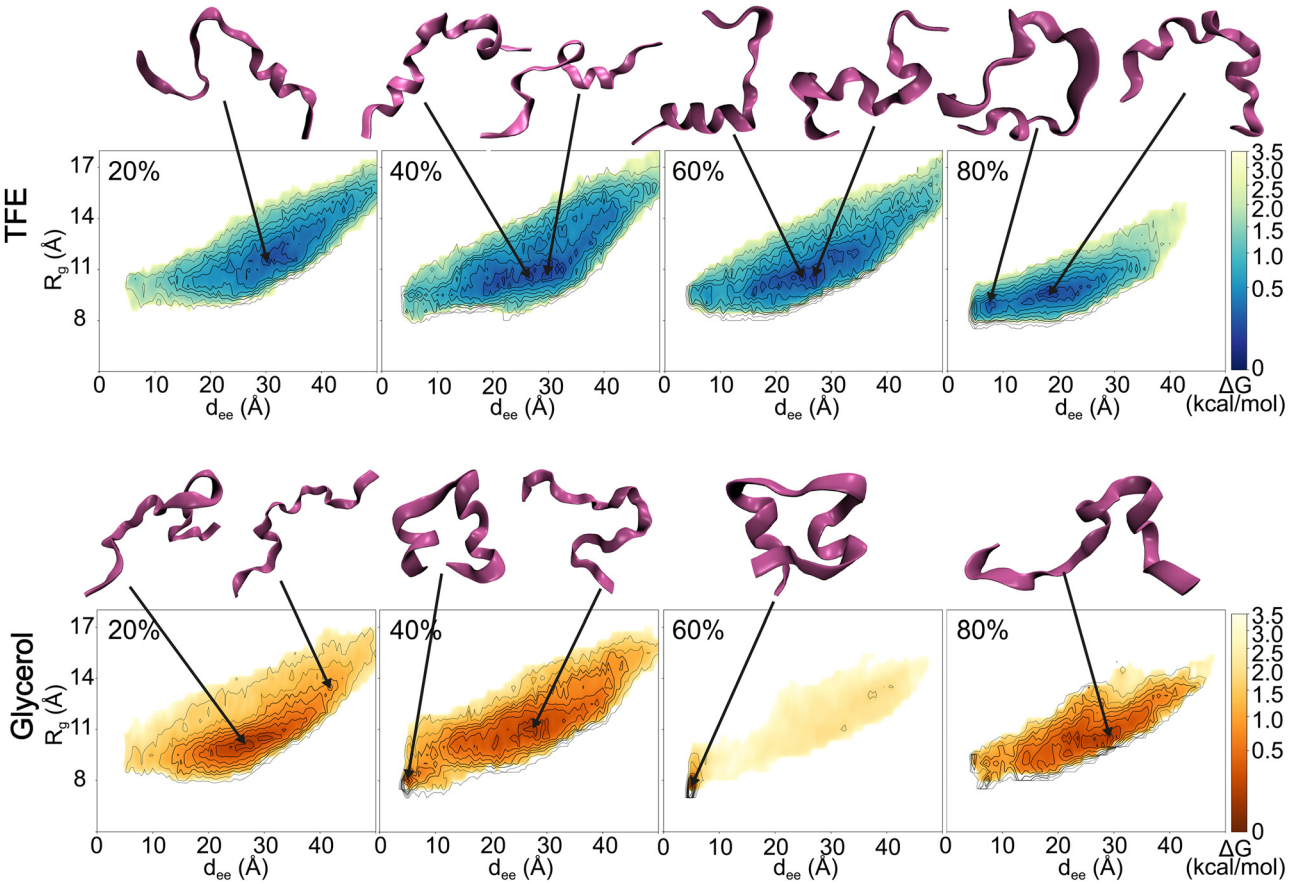

Fig. 3 Free-energy surfaces of the peptide projected onto the radius of gyration (R_g) and the N–C terminal distance for TFE–water (top row) and glycerol–water (bottom row) mixtures at increasing cosolvent concentrations (20%, 40%, 60%, and 80%). Color contours represent ΔG (kcal mol^{-1}) using a common energy scale across all panels.

below 10 Å and a radius of gyration near 8 Å. This structure contains a well-defined α-helical segment. At the same time, β-sheet-like conformations become favorable at N–C distances near 30 Å, indicating increased structural heterogeneity. At 60% glycerol–water (bottom row, third column), the energy landscape becomes dominated by a single compact minimum characterized by an N–C terminal distance of approximately 5 Å and a radius of gyration near 8 Å. This conformation resembles the compact state observed at 40% glycerol and involves partial encapsulation of the peptide by glycerol molecules. At 80% glycerol–water (bottom row, far right), compact conformations remain energetically favorable. However, the radii of gyration are slightly larger than those in TFE–water at the same concentration, and the ensemble retains structural heterogeneity with mixed secondary-structure features.

Overall, Fig. 3 shows that increasing glycerol concentration promotes peptide compaction and partial encapsulation, but does not produce the same progressive stabilization of uniform α-helical motifs observed in TFE.

3.2 Effect of the cosolvent on structure and interactions

3.2.1 Solvation differences govern secondary structure formation. In TFE–water mixtures, helicity increases systematically with increasing TFE content, consistent with the known helix-stabilizing effect of TFE.[16] This behavior is consistent with reduced backbone hydration and enhanced intramolecular hydrogen bonding. In glycerol–water mixtures, an increase in helical content is also observed with increasing glycerol concentration; however, the resulting conformational ensembles differ substantially (Fig. 3). TFE-rich environments favor helix–turn–helix motifs indicative of cooperative helix stabilization, whereas glycerol promotes helical segments primarily in the central region of the chain, accompanied by a significant population of β-sheet-like structures.

In general, as the concentration of cosolvent increases, creating a more dehydrating environment, the helicity of the conformational assemblies increases. This trend aligns with observations previously reported for P1LEA-22 under conditions of increasing salinity.[31] The helicity contribution per residue and the flexibility of the backbone were calculated for each composition of cosolvent (Fig. 4). Across both cosolvents and all concentrations, the terminal residues and their immediate neighbors exhibited high flexibility and low helicity. A distinct pattern emerged in the middle of the sequence, where residue 11 showed high flexibility while its helicity increased in proportion to the cosolvent ratio. Furthermore, while helicity generally increased with cosolvent concentration, the trends differed between mixtures: in the TFE–water system, higher

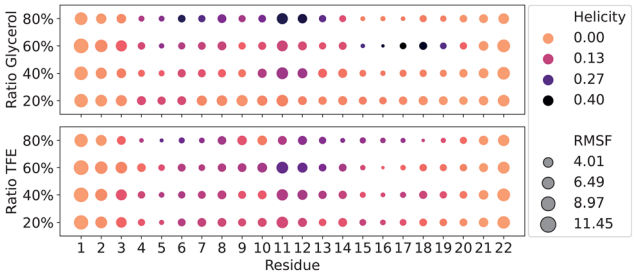

Fig. 4 Helicity and backbone flexibility across the peptide sequence at different solvent compositions. Residue-resolved helicity (color map) and RMSF (marker size) as a function of solvent composition.

ratios promoted helicity in specific residues (Fig. 4, bottom). In contrast, the glycerol–water mixture at 60% cosolvent showed a different set of residues contributing to the overall helicity (Fig. 4 top). Peptide conformational assembly is highly sensitive to both cosolvent concentration and chemical identity.

3.2.2 Solvation patterns and residue-specific interactions depend on cosolvent identity. To quantify differences in solvation, the average number of water oxygen atoms within 2.8 Å of each residue and cosolvent oxygen atoms (from TFE or glycerol) was calculated for the 80% TFE–water and 80% glycerol–water systems. Additionally, the average number of fluorine atoms (TFE) and carbon atoms (glycerol) within 5 Å of each residue was determined (Fig. 5). We observe that charged residues are surrounded by a larger number of water oxygen atoms in the TFE–water mixture, whereas direct interactions with TFE oxygen atoms are minimal. In glycerol–water, comparable numbers of oxygen atoms from both water and glycerol are observed around the peptide, indicating competition between glycerol and water for polar interactions. In addition, the hydrophobic moiety of TFE, represented by fluorine atoms, exhibits more extensive interactions with peptide residues than the carbon atoms of glycerol. Together, these results indicate that TFE is preferentially excluded from polar solvation sites and instead associates through hydrophobic interactions, whereas glycerol directly reshapes the local hydration shell by replacing water around charged residues.

To quantify electrostatic interactions, the distance between O–N atoms of charged residues pairs was calculated for each cosolvent and its ratio. In the TFE–water systems (Fig. 6 top), increasing TFE concentration leads to decrease the distance between the charged couple residues. Importantly, the distances between four characteristic couples of charged residues were identified to be close enough to attribute an electrostatic interaction: ASP3–LYS6, GLU11–LYS8, ASP14–LYS17, and GLU22–LYS19. Notably, these interactions occur in regions that retain helical secondary structure, predominantly near the chain termini. The separation between interacting residues is approximately three amino acids, consistent with the 3.6-residue periodicity of an α-helix. These observations suggest that increasing TFE concentration enhances electrostatic interactions that contribute to the stabilization of terminal helical segments in the P1LEA-22 peptide.

In glycerol–water, the distance between charged residues are close in the couples ASP3–LYS6, ASP14–LYS17, and GLU22–LYS19 (Fig. 6 bottom). These interactions also occur near the termini; however, no clear correlation is observed between the couples of residues and regions of high helical content. Importantly, the identities of the dominant electrostatic interaction largely overlap with those found in TFE–water, suggesting that their formation is primarily driven by reduced water availability rather than by helix stabilization itself.

Collectively, these findings indicate that while both cosolvents enhance electrostatic interactions under limited water availability, only TFE effectively couples these interactions to cooperative helix stabilization. To support this mechanism, we evaluated the free-energy landscape projected in LYS6-ASP3 donor–acceptor distances at low and high cosolvent concentrations. At 20%

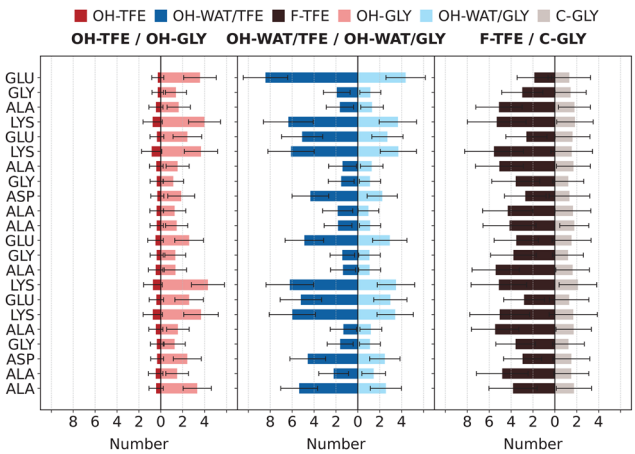

Fig. 5 Solvent coordination for each residue in 80% TFE–water and 80% glycerol–water mixtures. The three panels show cosolvent oxygen interactions, water oxygen interactions, and hydrophobic contacts from TFE fluorine and glycerol carbon atoms. Bars represent average coordination numbers with standard deviation.

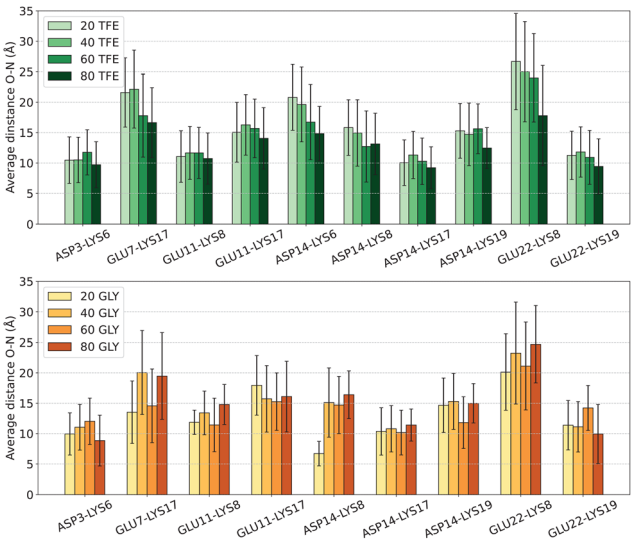

Fig. 6 Average distance between nitrogen and oxygen atoms of the charged residues couples at different cosolvent concentration.

cosolvent, the donor acceptor distances remain fluctuating within a non-structured state. At 80% concentration, both landscapes present minimums at short distances, d_{O-N} around 4–6 Å), and low helicity, suggesting that desolvation drives the electrostatic interactions independently of folding. Furthermore, the landscapes clarify the behavior observed under limited water conditions where in glycerol the peptide presents low helical content while maintaining short distances. In contrast, 80% TFE landscape exhibits a continuous low energy pathway connecting short donor–acceptor distances with highly helical conformations, indicating that electrostatic interactions and helix formation are more strongly coupled in TFE-rich environments.

4 Discussion

Our results demonstrate that solvent identity and concentration profoundly reshape the conformational landscape of the model peptide through distinct solvation mechanisms. The interactions between water, TFE, and glycerol modulate both global structural descriptors—such as N–C terminal distance and radius of gyration—and residue-level solvation patterns that ultimately determine secondary structure formation. This is consistent with the known behavior of disordered model peptides, which undergo significant structural transitions and gain secondary structure in response to changes in hydration and solvent type to mimic dehydration.[15]

At low cosolvent concentration (20%), both TFE and glycerol maintain the peptide in largely disordered and relatively extended conformations. Charged residues remain predominantly hydrated by water, indicating that neither cosolvent significantly perturbs backbone hydration or electrostatic screening at this concentration. Consequently, secondary structure formation remains limited, and the conformational ensemble resembles that observed in aqueous solution. This behavior is consistent with previous observations that demonstrate how moderate levels of fluorinated alcohols only weakly perturb the conformational equilibrium of unfolded peptides before preferential interactions become dominant at higher concentrations.[32,33]

At intermediate concentration (40%), structured fragments are stabilized. Both solvents support conformations within similar ranges of terminal distance and radius of gyration; however, their structural preferences diverge. Glycerol facilitates β-sheet-like conformations in more extended states (30 Å terminal distance), whereas TFE promotes early α-helical stabilization. The helix-promoting effect of TFE has been extensively documented and is commonly attributed to preferential solvation and partial dehydrogenation of the peptide backbone, which favors intramolecular hydrogen bonding and shifts the helical–coil equilibrium toward the helical state.[33,34] Importantly, our observed atomistic helical transitions qualitatively match the macroscopic structural shifts reported in circular dichroism (CD) studies of LEA-derived model peptides under water limitation.[11,17] Notably, the 40% glycerol–water system also populates a distinct low-energy compact state (N–C distance <10 Å, R_g 8 Å), suggesting that glycerol can induce substantial compaction without fully enforcing a specific secondary motif. This behavior underscores the different physicochemical influences of the two cosolvents.

At 60%, the divergence becomes more pronounced. Glycerol favors a dominant compact state characterized by extensive solvent encapsulation, consistent with excluded volume effects and competitive hydrogen bonding that reduce backbone flexibility. That is consistent with previous reports where polyols, such as glycerol, are known to stabilize compact protein states by shifting the equilibrium toward conformations with reduced solvent accessible surface area through preferential exclusion from the protein surface.[35] And the structural compaction observed at high concentration of glycerol correlates with the conformational behavior observed experimentally for other members of the LEA protein family.[18] In contrast, TFE supports multiple conformational states over a broader structural range. Its amphipathic character enables selective interactions with hydrophobic residues while allowing the retention of internal water molecules near charged groups. Such preferential interactions create a locally reduced dielectric environment that favors intrapeptide hydrogen bonding and promotes helix formation[34,36] This balance allows TFE to promote helix formation without complete solvent exclusion.

At high concentrations (80%), both cosolvents dominate the peptide solvation shell; however, their structural outcomes remain distinct. TFE induces compact conformations with cooperative helix–turn–helix motifs and enhanced stabilization of electrostatic interactions. The preservation of partial hydration around charged residues suggests reduced dielectric screening combined with strengthened intramolecular electrostatic interactions, which can further stabilize helical conformations in fluorinated alcohol environment.[33] In contrast, glycerol produces compact yet structurally heterogeneous ensembles, characterized by reduced water availability around charged residues and a broader distribution of secondary structures. Transition towards more ordered states have been observed in LEA proteins, where the loss of water acts as primary driver for reducing the conformational space and stabilizing specific structural motifs.[3]

The solvation analysis provides mechanistic insight into these differences. TFE is preferentially excluded from polar solvation sites and interacts primarily through hydrophobic association, thereby promoting backbone hydrogen bonding and coupling electrostatic interactions to helix stabilization. Glycerol, in contrast, competes directly with water in the first solvation shell and exerts a more global compaction effect through steric restriction and hydrogen bond redistribution rather than helix-specific stabilization. Such behavior is consistent with the general mechanism of polyol-induced protein stabilization through preferential hydration and the entropic crowding effect.[35]

Overall, the folding behavior of the model peptide is highly solvent dependent. TFE drives cooperative helix stabilization through a combination of preferential exclusion, hydrophobic association, and enhanced intrahelical electrostatics. Glycerol

promotes compaction *via* competitive solvation and excluded volume effects but does not couple electrostatic interactions to a specific secondary structure. These findings highlight how different cosolvent properties can differentially modulate peptide conformational landscapes, providing molecular-level insight into solvent-induced folding mechanisms.

Direct experimental structural characterization of P1LEA-22 under the exact mixture ratios studied here is currently unavailable. Therefore, although our simulations reproduce trends consistent with experimental observations for LEA peptides under reduced water availability, the lack of direct structural validation remains a limitation of the present study. Future targeted experiments will be valuable to further test the structural assignments proposed here.

The simulations reported here rely on non-polarizable classical force fields, which approximate weakly polar intra-peptide and intermolecular noncovalent interactions through fixed partial charges and Lennard-Jones parameters. Therefore, electronic polarizability, charge redistribution, and quantum-mechanical contributions to dispersion are not treated explicitly. These approximations may affect the quantitative description of dense mixed-solvent environments. Nevertheless, the use of classical molecular dynamics enables extensive sampling of peptide conformational ensembles over microsecond timescales, allowing us to compare relative solvent-dependent trends across the same simulation framework.

5 Conclusion

This study demonstrates that the conformational landscape of the P1LEA-22 model peptide is highly sensitive to the physicochemical properties of the surrounding medium. Using Gaussian Accelerated Molecular Dynamics (GaMD), we provide an atomistic description of how TFE and glycerol, although both mimic dehydration, drive peptide folding through distinct mechanisms.

TFE acts as a strong helix-inducing cosolvent and nanocrowding agent. At high concentrations (80%), it stabilizes a well-defined helix–turn–helix motif, accompanied by increased frequency of intrahelical electrostatic interactions such as GLU11–LYS8 and GLU22–LYS19. These results indicate that TFE promotes cooperative helix stabilization by enhancing intramolecular electrostatic interactions while associating with hydrophobic regions of the peptide.

In contrast, glycerol competes directly with charged residues for hydrogen bonding and induces compaction without enforcing a single dominant secondary structure. The resulting ensemble includes localized helices and β-sheet-like conformations, reflecting a distinct mechanism driven by competitive solvation and excluded volume effects. Importantly, electrostatic interactions in both media primarily arise from reduced water availability rather than being solely a consequence of helix formation.

Together, these findings provide molecular-level insight into how solvent-specific interactions regulate structural transitions in Group-3 LEA proteins. The different mechanisms uncovered here help explain how these intrinsically disordered proteins adapt to extreme dehydration while preserving structural and functional integrity.

Author contributions

IP-T: conceptualization, methodology, formal analysis, investigation (molecular dynamics simulations), and writing – original draft. LD: conceptualization, methodology, formal analysis, supervision, and writing – review & editing.

Conflicts of interest

The authors declare no competing interests.

Data availability

The data of this work is available in Zenodo repository with the DOI: https://doi.org/10.5281/zenodo.20433796. The Zenodo repository is organized as follows, where the term COSOLVENT represents either TFE (trifluoroethanol) and GLY (glycerol): Unit_boxes/COSOLVENT/PatamererCOSOLVENT_files: Contains the parameter files required to describe both TFE and glycerol. Unit_boxes/COSOLVENT/Boxes_after_simulations: Includes the equilibrated unit box configurations in PDB format, which serve as building block to construct the complete solvated system. Unit_boxes/Example_build_unit_box_packmol: Contain an example template for the generation of unit box, providing the Packmol script and necessary PDB files. PILEA-22/COSOLVENT/XX_percentage: Contains the topology files (sis.parm7), initial coordinates files (sis.rst7), production trajectory files of each 100 steps (04_npt_prodgamd_100steps.nc), and the GaMD log files (gamd.log) containing the boost data. PILEA-22/Inputs: contains all inputs files required to reproduce the entire simulation workflow, from minimization to production. These files are ready to be executed alongside the respective topology (sis.parm7) and coordinate (sis.rst7) files of each system. PILEA22/Reweighting: includes the Reweighting_workflow file with the exact command lines used to perform the reweighting and free energy calculations *via* the PyReweighting2D.py script from Mio lab.

Supplementary information (SI) is available. See DOI: https://doi.org/10.1039/d6cp00960c.

Acknowledgements

Itzel Pérez-Trejo (No. 771096) is grateful to CONAHCyT for the fellowships granted. This research was funded by Universidad Nacional Autonoma de Mexico institutional programs: Dirección General de Cómputo y de Tecnologías de Información (LANCAD-UNAM-DGTIC-306), Programa de Apoyo a Proyectos de Investigación e Innovación Tecnológica (PAPIIT – IN208025), and Programa de Apoyo a la Investigación y el Posgrado (PAIP – 5000-9155).

References

1 L. Dure and C. Chlan, *Plant Physiol.*, 1981, **68**, 180–186.
2 K. Goyal, L. J. Walton and A. Tunnacliffe, *Biochem. J.*, 2005, **388**, 151–157.
3 A. V. Popova, S. Rausch, M. Hundertmark, Y. Gibon and D. K. Hincha, *Biochim. Biophys. Acta, Protein Struct.*, 2015, **1854**, 1517–1525.
4 J. L. Reyes, M.-J. Rodrigo, J. M. Colmenero-Flores, J.-V. Gil, A. Garay-Arroyo, F. Campos, F. Salamini, D. Bartels and A. A. Covarrubias, *Plant, Cell Environ.*, 2005, **28**, 709–718.
5 N. Bies-Ethève, P. Gaubier-Comella, A. Debures, E. Lasserre, E. Jobet, M. Raynal, R. Cooke and M. Delseny, *Plant Mol. Biol.*, 2008, **67**, 107–124.
6 A. Banerjee and A. Roychoudhury, *Plant Growth Regul.*, 2015, **79**, 1–17.
7 M. Battaglia, Y. Olvera-Carrillo, A. Garciarrubio, F. Campos and A. A. Covarrubias, *Plant Physiol.*, 2008, **148**, 6–24.
8 S. Koubaa, A. Bremer, D. K. Hincha and F. Brini, *Sci. Rep.*, 2019, **9**, 3720.
9 B. M. LeBlanc and S. C. Hand, *Biochim. Biophys. Acta, Proteins Proteomics*, 2021, **1869**, 140642.
10 L. Dure III, *Plant J.*, 1993, **3**, 363–369.
11 T. Shimizu, Y. Kanamori, T. Furuki, T. Kikawada, T. Okuda, T. Takahashi, H. Mihara and M. Sakurai, *Biochemistry*, 2010, **49**, 1093–1104.
12 T. Furuki, T. Shimizu, S. Chakrabortee, K. Yamakawa, R. Hatanaka, T. Takahashi, T. Kikawada, T. Okuda, H. Mihara, A. Tunnacliffe and M. Sakurai, *Biochem. Biophys. Acta*, 2012, **1824**, 891–897.
13 T. Furuki and M. Sakurai, *Biochem. Biophys. Acta*, 2014, **1838**, 2757–2766.
14 T. Furuki and M. Sakurai, *Biochim. Biophys. Acta*, 1864, 1237–1243.
15 T. Furuki, T. Niwa, H. Taguchi, R. Hatanaka, T. Kikawada and M. Sakurai, *Biochem. Biophys. Rep.*, 2019, **17**, 27–31.
16 M. Goodman, I. Listowsky, Y. Masuda and F. Boardman, *Biopolymers*, 1963, **1**, 33–42.
17 R. M. Culik, R. M. Abaskharon, I. M. Pazos and F. Gai, *J. Phys. Chem. B*, 2014, **118**, 11455–11461.
18 A. Bremer, M. Wolff, A. Thalhammer and D. K. Hincha, *FEBS J.*, 2017, **284**, 919–936.
19 C. Navarro-Retamal, A. Bremer, J. Alzate-Morales, J. Caballero, D. K. Hincha, W. GonzÃ¡lez and A. Thalhammer, *Phys. Chem. Chem. Phys.*, 2016, **18**, 25806–25816.
20 I. Pérez-Trejo and L. Dominguez, *J. Mol. Model.*, 2023, **29**, 198.
21 L. MartÃnez, R. Andrade, E. G. Birgin and J. M. MartÃnez, *J. Comput. Chem.*, 2009, **30**, 2157–2164.
22 J. Wang, W. Wang, P. A. Kollman and D. A. Case, *J. Mol. Graph. Model.*, 2006, **25**, 247–260.
23 J. Wang, R. M. Wolf, J. W. Caldwell, P. A. Kollman and D. A. Case, *J. Comput. Chem.*, 2004, **25**, 1157–1174.
24 S. Piana, A. G. Donchev, P. Robustelli and D. E. Shaw, *J. Phys. Chem. B*, 2015, **119**, 5113–5123.
25 D. Case *et al.*, *AMBER 2018*, Universidad de California, San Francisco, 2018.
26 J.-P. Ryckaert, G. Ciccotti and H. J. Berendsen, *J. Comput. Phys.*, 1977, **23**, 327–341.
27 T. Darden, D. York and L. Pedersen, *J. Chem. Phys.*, 1993, **98**, 10089–10092.
28 G. Lamm and A. Szabo, *J. Chem. Phys.*, 1986, **85**, 7334.
29 J. Yang, R. Yan, A. Roy, D. Xu, J. Poisson and Y. Zhang, *Nat. Methods*, 2015, **12**, 7–8.
30 Y. Miao, W. Sinko, L. Pierce, D. Bucher, R. C. Walker and J. A. McCammon, *J. Chem. Theory Comput.*, 2014, **10**, 2677–2689.
31 D. Léon, M. P. Vermeuel, P. Gupta and M. R. Bunagan, *J. Pept. Sci.*, 2020, **26**, e3247.
32 C. L. Cuevas-Velazquez, G. Saab-Rincon, J. L. Reyes and A. A. Covarrubias, *J. Biol. Chem.*, 2016, **291**, 10893–10903.
33 J. K. Myers, C. Nick Pace and J. Martin Scholtz, *Protein Sci.*, 1998, **7**, 383–388.
34 J. Vymětal, L. Bednárová and J. Vondrášek, *J. Phys. Chem. B*, 2016, **120**, 1048–1059.
35 V. Vagenende, M. G. S. Yap and B. L. Trout, *Biochemistry*, 2009, **48**, 11084–11096.
36 M. J. Bodkin and J. M. Goodfellow, *Biopolymers*, 1996, **39**, 43–50.

